Chapter II

Experimental Principles and Approaches

***Overview of the chapter*:**

In this chapter, the preparation method of CdSe nanocrystals, as well as the experimental principles and approaches of optical, powder X-ray diffraction, extended X-ray absorption fine structure, and photoemission experiments are introduced.

2.1 Preparation of CdSe nanocrystals by colloidal method

2.1.1 *CdSe nanocrystals passivated with TOPO/HDA*

CdSe NCs were prepared following the organometallic synthesis procedure in an air-free environment [1-3]; the schematic diagram of preparation method is shown in Fig. 2.1. Firstly, CdO of 51.4 mg (0.4 mmol) was dissolved in the mixture of trioctylphosphine oxide (TOPO) of 1.15 mL and hexadecylamine (HDA) of 2.85 mL. This mixture is placed in a three-neck flask and heated to ~270 ˚C under purified argon flow. Adequate oleic acid (OA) or octyl-phosphonic acid (OPA) of 230 μL (0.8 mmol) was injected into the

mixture to form the cadmium precursor with a color varying from dark red to transparent. Meanwhile, the TOPSe was prepared by mixing Se pellets of 59.22 mg (0.75 mmole) with trioctylphosphine (TOP) of 2.5 mL and maintained at 190 ˚C. Then the TOPSe solution was rapidly injected into the Cd precursor. By controlling the reaction time and growth conditions, the TOPO/HDA-capped CdSe NCs in various sizes can be obtained. All samples were immediately cooled to stop particle growth. The colloid was then dissolved in toluene and methanol to further purify by size-selective precipitation. This purification process was repeated for several times so that a very narrow size distribution can be achieved.

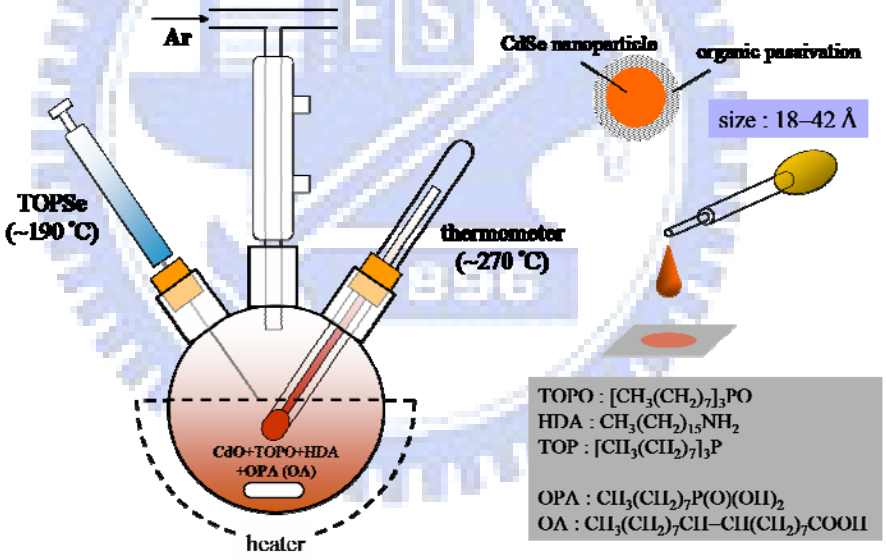

FIG. 2.1: The schematic representation of the organometallic preparation of CdSe NCs using TOPO, HDA, and TOP.

2.1.2 *CdSe nanocrystals treated with pyridine*

The surface of NCs can be modified by repeated exposure to an excess of a

competing capping group. Pyridine-treated CdSe NCs were obtained by refluxing the CdSe/TOPO/HDA NCs in pyridine solvent for 2−4 hours at 60−70 ˚C. After that, the NCs can well disperse in pyridine and show a dramatic reduction in their photoluminescent intensity.

2.2 TEM and optical characterization

2.2.1 *Transmission electron microscopy*

Figure 2.2(a) shows transmission electron microscope (TEM) image of TOPO/HDA-passivated CdSe NCs, these particles are well dispersed and do not touch each other. After CdSe NCs treated by pyridine [see Fig. 2.2(b)], the particles reveal aggregated and touch each other.

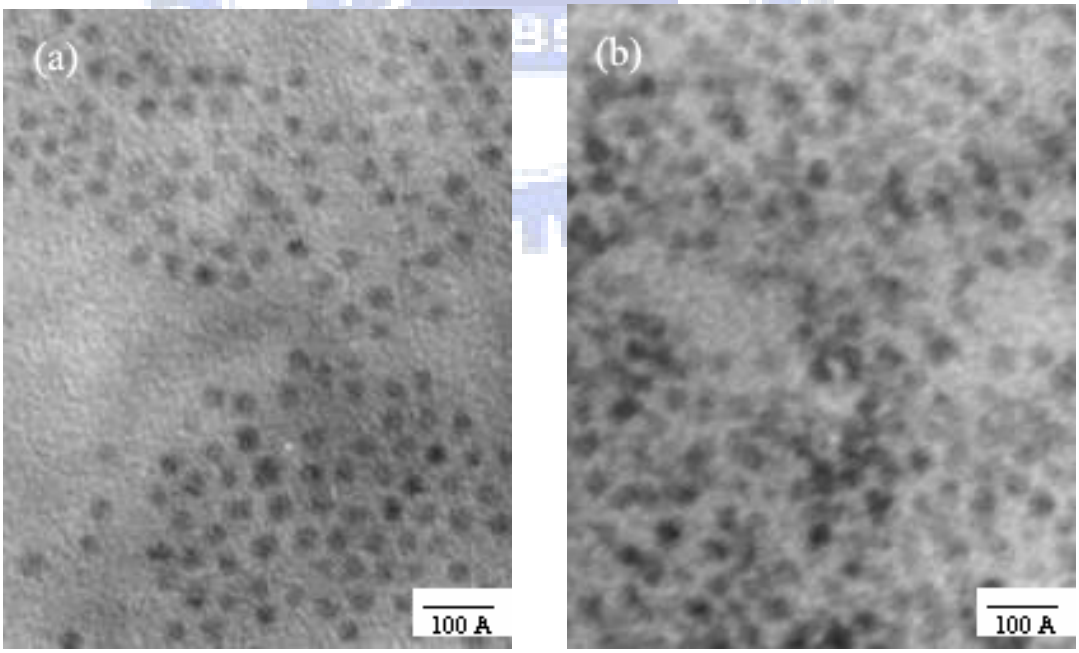

FIG. 2.2: (a) TEM image in bright field with lattice contrast shows a collection of slightly prolate particles. (b) NCs deposited from pyridine appear aggregate, revealing possible interaction of particle with its neighbors.

Figure 2.3 represents the size distribution histograms of major and minor diameters, determined from TEM measurements [Fig. 2.2(a)], for CdSe NCs passivated with TOPO/HDA. NCs have an ellipsoid shape with an aspect ratio of ~1.2, and their size distribution is about ±2 Å. We found that the aspect ratio (1.1–1.3) slightly increases as the growth of NCs (18–42 Å). In this study, the mean diameter of NCs is defined by $(D_{major} \times D_{\min or}^2)^{1/3}$.

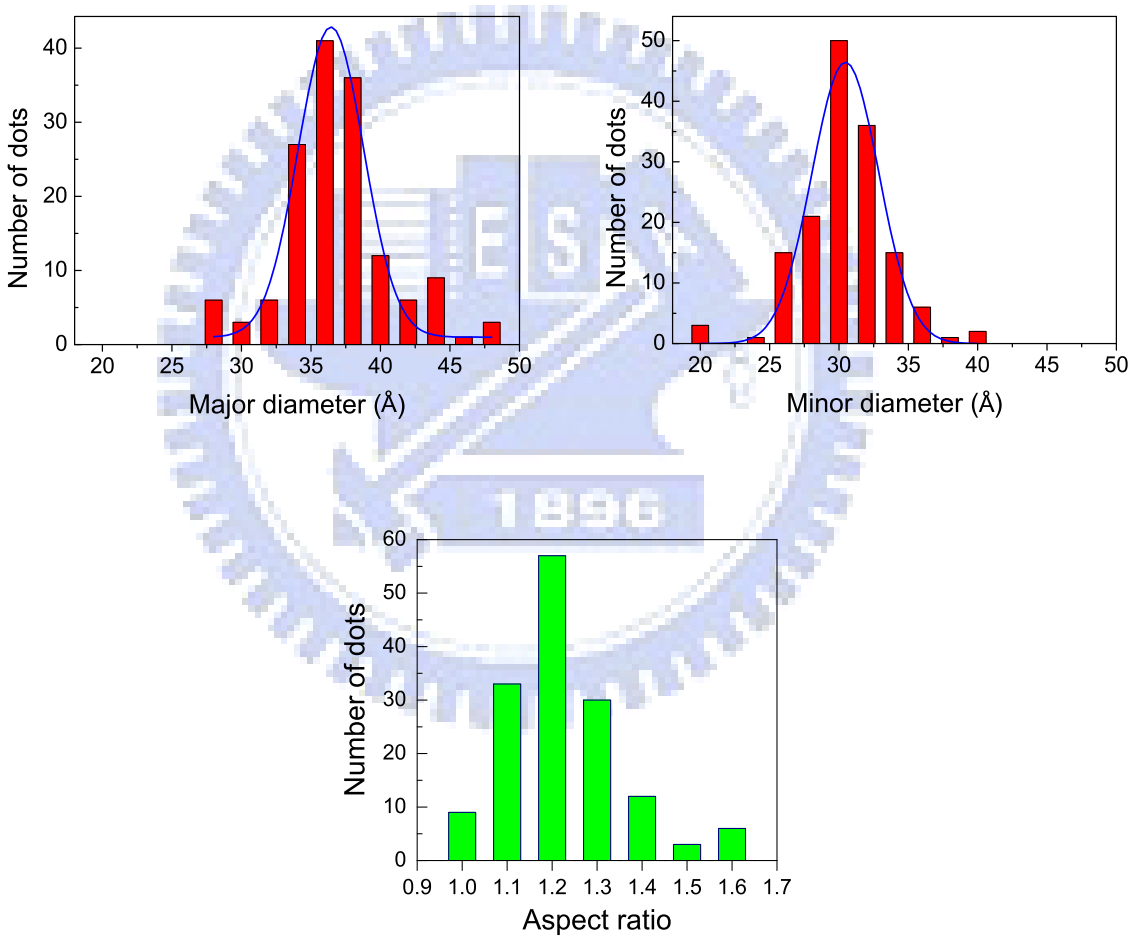

FIG. 2.3: Size histograms of CdSe NCs determined from TEM image represented in Fig. 2.2(a) for 150 particles.

2.2.2 *Optical characterization*

Optical absorption spectra were taken at room temperature on a Hewlett-Packard Agilent-8453 spectrophotometer in a transparent solution with low optical density, prepared by dissolving less than 1 mg of NC powder in 3 mL of toluene, using 1-cm quartz cuvettes. Luminescent spectra were collected between 400 and 750 nm at room temperature on a Hitachi F-4500 spectrometer. Typical ultraviolet-absorption (UV-absorption), PL, and PL excitation (PLE) spectra of CdSe NCs are shown in Fig. 2.4. The inset represents the first absorption peak as a function of mean diameter, which agrees with published literature [4].

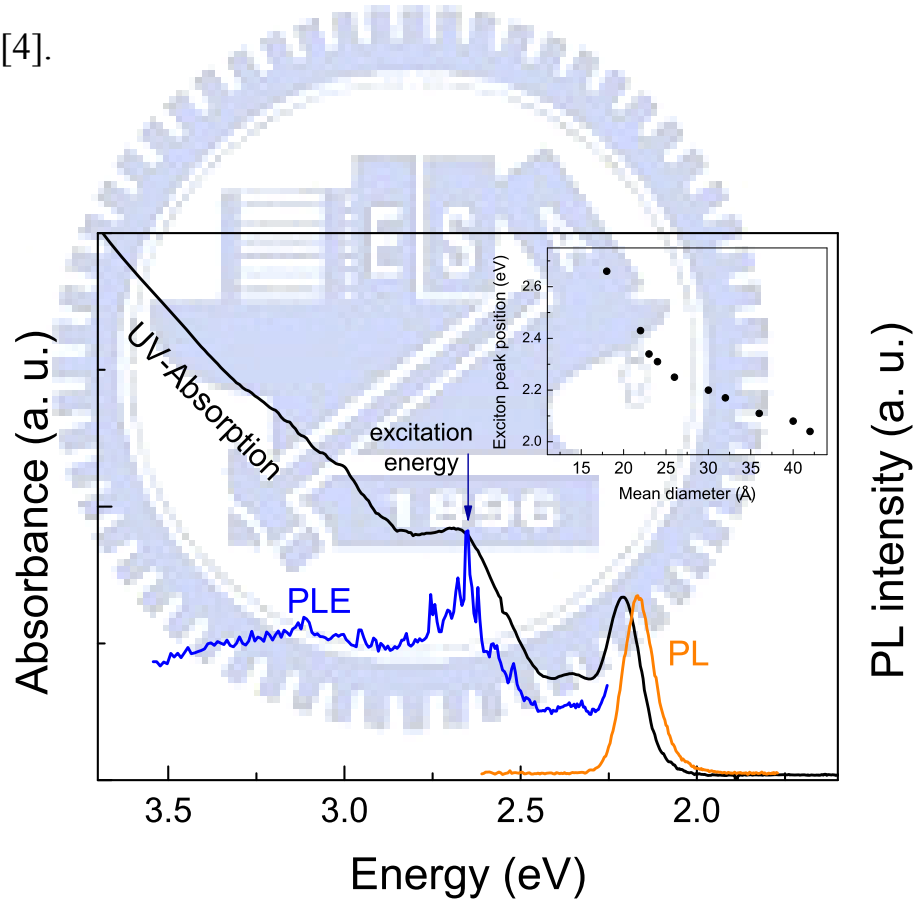

FIG. 2.4: Optical spectra of CdSe nanocrystals with mean diameter of ~30 Å. The inset shows the first-absorption peak position as a function of nanocrystal size estimated by TEM.

Figure 2.5 displays the wide spectral range of luminescence from CdSe NCs. The photograph shows five different samples of CdSe NCs dispersed in dilute

toluene solutions. As the size of CdSe NCs increases, the color of the luminescence shows a continuous progression from blue to red.

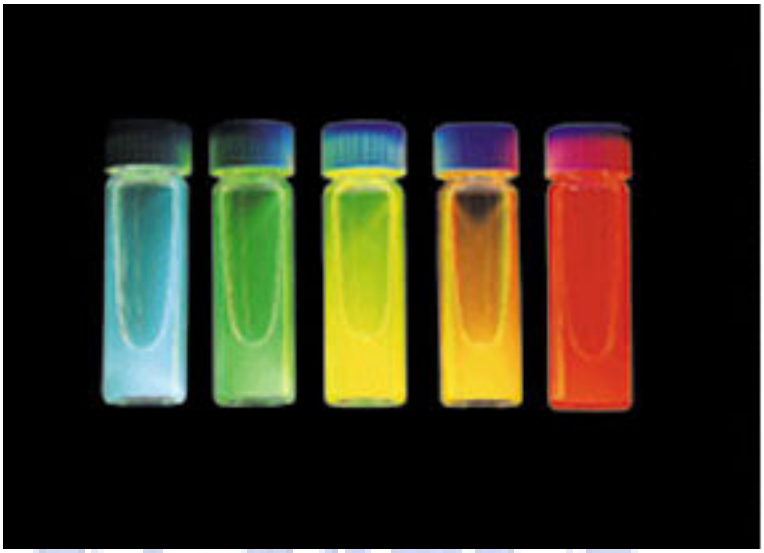

FIG. 2.5: Color photograph demonstrates the wide spectral range of bright fluorescence from different size samples of CdSe nanocrystals.

2.3 X-ray diffraction

2.3.1 *Powder X-ray diffraction from small crystallites*

X-ray diffraction is a versatile, non-destructive technique that reveals detailed information about the crystallographic structure and chemical composition of natural and manufactured materials. According to the peak positions, the lattice parameters can be determined and the structural phase was identified through comparison with known standards. The relative peak intensities contain information about the particle shape and stacking sequence, while the linewidths reveal information about the particle size and crystalline order [5].

X-rays are the general term used to describe electromagnetic radiation with wavelengths between roughly 0.1 Å and 100 Å. This is shorter than ultraviolet but longer than gamma radiation. The spacing of adjacent atoms in a crystal structure is typically about 3 Å. The wavelengths of X-rays are therefore of the same order as the atomic spacing in a crystal. In 1912, Max von Laue realized that a crystalline sample should therefore cause X-rays to diffract and indeed proved this to be the case. Subsequently, W. L. Bragg produced a simple geometrical interpretation, making it easy to relate the angle of diffraction to the interplanar spacing.

A common laboratory source of X-rays consists of an evacuated tube in which electrons are emitted from a heated tungsten filament, and accelerated by an electric potential (typically several tens of kilovolts) to impinge on a water-cooled metal target. The interaction between the electrons and the target leads to the emission of X-rays: some radiations have a wavelength characteristic of the target, and some have a continuous distribution of wavelengths (the so-called "white radiation" or “bremsstrahlung”). X-rays in the practical are obtained from a copper source (Cu K_α radiation = 8047 eV). For most experiments, characteristic radiation is selected (using a filter or Bragg reflection from a suitable crystal) because of its intensity and accurately known wavelength. A synchrotron can also be used to generate X-rays of very high intensity. The radiation produced in a synchrotron is continuous in photon energy and is monochromatic and variable energies for different experiments.

In a powder XRD experiment, the reciprocal space denotes a uni-dimensional plot of the diffracted intensity $I(q)$ as a function of the scattering vector $q = 4\pi \sin\theta / \lambda$, in which θ is the Bragg angle and λ is the wavelength of the

incident light. For a crystalline material, the position of the diffracted peaks is determined by the lattice parameters *a*, *b*, *c*, α, β, and γ, while the relative peak intensity depends on the spatial location of atoms within the unit cell. If the rigorous three-dimentional periodicity of an infinite crystal is missing due to defects in the irradiated specimen, the diffraction peaks will be consequently modified [5,6]. In the powder XRD literature, the types of defects are catalogued according to their effect on the patterns. In particular, the defects due to the reduction of the crystal size (grain size or crystallite size effect, including also dislocations) result in a broadening of the diffraction pattern of that substance.

Another type of defect results from deviations of the interplanar distances with respect to their mean value (strain). This kind of defect causes a line broadening which is dependent upon the order of reflections, and generally it increases as a function of the reciprocal space variable q_{hkl}. In the case of inclusions in the matrix of small quantities of an extra-element and of residual stress, the peak positions may be shifted with respect to their ideal positions in a perfect crystal. Moreover, planar stacking faults may affect the peak shape in terms of asymmetry and peak shifts [7].

Supposed the sample with a random orientation including gases, liquids, amorphous solids, and crystalline powders, there can be any number of different kinds of atoms in the sample. The intensity from the sample is given by summing the amplitude of scattering from all atoms in the scattering volume, and then multiplying this sum by its complex conjugate [7]:

$$I = \sum_m f_m \exp\left[\frac{2\pi i}{\lambda}(\vec{k} - \vec{k}_0)\cdot\vec{r}_m\right]\sum_n f_n \exp\left[-\frac{2\pi i}{\lambda}(\vec{k} - \vec{k}_0)\cdot\vec{r}_n\right], \qquad (2.1)$$

where $\vec{r}_m$ is the instantaneous position of each atom *m*.

This expression is the same as that used for the intensity from a crystal. In that

case, however, each of the sums was a geometric progression, and the sums could be evaluated. Despite the expression must be left as a double sum, it is simpler to write it in terms of the difference vector $\vec{r}_{mn} = \vec{r}_m - \vec{r}_n$:

$$I = \sum_m \sum_n f_m f_n \exp\left[\frac{2\pi i}{\lambda}(\vec{k} - \vec{k}_0)\cdot \vec{r}_{mn}\right]. \tag{2.2}$$

When this array of atoms, considered as a rigid body, is allowed to take with equal probability all orientations in space, one can find the average intensity. Since each vector $\mathbf{r}_{mn}$ takes all orientations, its terminal point takes with equal probability all positions on the sphere of Fig. 2.6. In term of q, the average for each exponential term is given by

$$\langle \exp\left[\frac{2\pi i}{\lambda}(\vec{k} - \vec{k}_0)\cdot \vec{r}_{mn}\right]\rangle = \frac{1}{4\pi r_{mn}^2}\int_{\phi=0}^{\pi} e^{iqr_{mn}\cos\phi} 2\pi r_{mn}^2 \sin\phi d\phi = \frac{\sin qr_{mn}}{qr_{mn}}. \tag{2.3}$$

Using this value for each of the terms in Eq. (2.2), we obtain a very general and important equation for the average unmodified intensity from an array of atoms which takes all orientations in space:

$$I = \sum_m \sum_n f_m f_n \frac{\sin qr_{mn}}{qr_{mn}}, \tag{2.4}$$

which is called the *Debye equation* [5]. We should note that it involves only the magnitudes of the distances r_{mn} of each atom from every other atom.

For diffraction by nanocrystals, the effects such as small domain size, strains, and faulting are considerable on the diffraction pattern. The intensity from a single small parallelopipedon crystal [7] is given by

$$I = I_e F^2 \prod_{i=1}^{3} \frac{\sin^2(\pi/\lambda)(\vec{k} - \vec{k}_0)\cdot N_i a_i}{\sin^2(\pi/\lambda)(\vec{k} - \vec{k}_0)\cdot a_i}, \tag{2.5}$$

where I_e is related to the intensity of a primary beam, F is the structural factor, and N_i is the number of unit cells along the a_i direction. For a perfect crystal, the

N_i is a large number. Each of the three quotients differs from zero only if the three Laue equations are closely satisfied, and hence the powder pattern reflections are sharp. For very small crystals, in contract, N_i is small and the three quotients broaden so that the smaller the crystals the broader the reflections of powder pattern. The peak width can be expressed in terms of the crystallite size, and hence a measurement of the peak width provides a simple method for determining crystallite sizes.

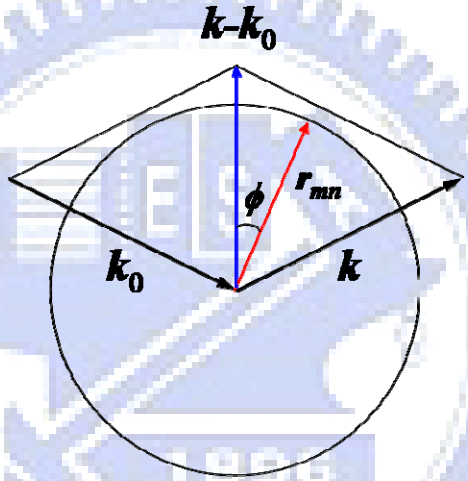

FIG. 2.6: Relations involved in letting the $\boldsymbol{r}_{mn}$ vector take all orientations in space [7].

If structural defects present, then the variation in structure factor within a crystallite must be taken into account. The effect on line width is similar to that due to crystallite size, but peak asymmetry or displacement can also be introduced. A common form of defect is the stacking fault, which occurs in 'layer structures', such as some silicates and graphite, where the forces holding layers together are much less than those within layers. Wilson gives a detailed treatment of defects in general and there is an admirable account by Warren of defects which can occur in f.c.c., b.c.c, and h.c.p. materials [7]. In general, the

contribution to the integral breadth is simply proportional to the probability of the occurrence of a defect [6]. The constant of proportionality depends on the nature of the defect and on *hkl*.

2.3.2 *Powder X-ray diffraction experiments*

Powder XRD spectra were collected on a diffractometer operating in the Bragg configuration using Cu K_α radiation (~8 keV X rays), as shown in Fig. 2.7. The accelerating voltage was set at 50 kV with 200 milliamp flux. Scatter and diffraction slits of 0.5° and a 0.1 mm collection slit were used. The NC powder samples for diffraction measurements were obtained by drop casting the dispersion of CdSe NCs with toluene on a silicon wafer and then slowly evaporating the solvent. The silicon substrate was used to decrease the X-ray scattering background.

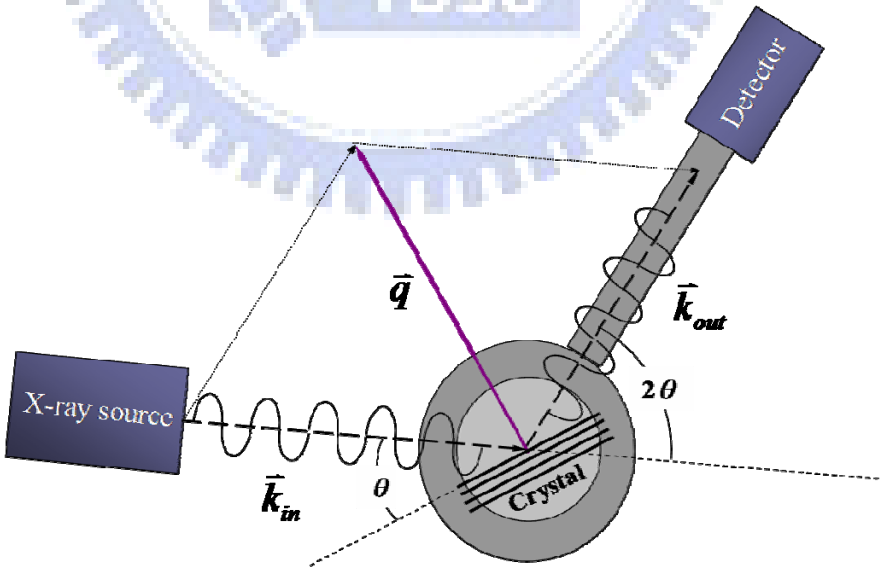

FIG. 2.7: Schematic representation of X-ray diffraction apparatus used in conventional mode.

2.4 X-ray absorption spectroscopy

2.4.1 *Synchrotron radiation*

When charged particles travel at relativistic velocities (close to the speed of light) in applied magnetic fields which force them to orbit along a curved paths, photons are emitted in a narrow cone in the forward direction, at a tangent to the orbit. In a high-energy electron or positron storage ring these photons are electromagnetic radiation with a continuous wavelength, ranging from infrared to X-rays. This radiation is referred to as "*synchrotron radiation*".

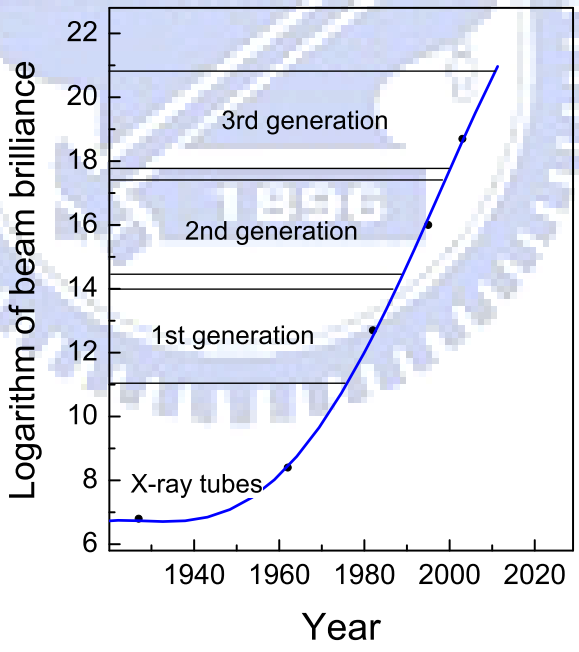

FIG 2.8: The brilliance of X-ray sources as a function of time.

X-rays were discovered by W. C. Röntgen in 1895, which have been developed to be a powerful tool for scientific research, including materials,

physics, chemistry, industry, biology, medicine, and so on. By means of synchrotron radiation with high brightness, all facets of X-ray research have been revolutionized. Figure 2.8 shows the rapid increase in the brightness of X-ray beams available for research, since the introduction of synchrotron radiation in the 1960's [8].

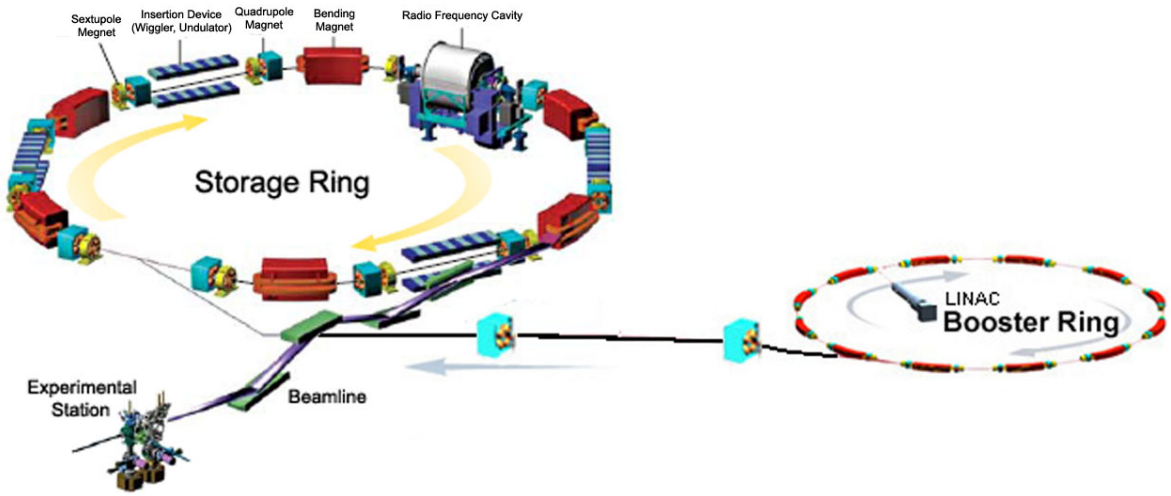

FIG 2.9: Schematic representation of the accelerator and experimental facilities at the NSRRC, the Taiwan Light Source.

First generation synchrotron sources were high-energy physics accelerators, where the synchrotron radiation was an unwanted by-product. In the 1960s, physicists and chemists began to use the radiation from several of these accelerators in a "parasitic mode". The second generation of synchrotron radiation facilities, such as the National Synchrotron Light Source in USA, were constructed expressly to provide synchrotron X-rays for research. The third generation storage rings have long straight sections for the installation of insertion devices (wigglers and undulators) to provide even higher brightness photon beams. The Taiwan Light Source at National Synchrotron Radiation

Research Center (NSRRC), which is one of the earliest third-generation synchrotron light source facilities, began to operate in 1993; a diagram of the facilities are shown in Fig. 2.9. The bright spectra from NSRRC light sources as well as conventional X-ray source are plotted in Fig. 2.10.

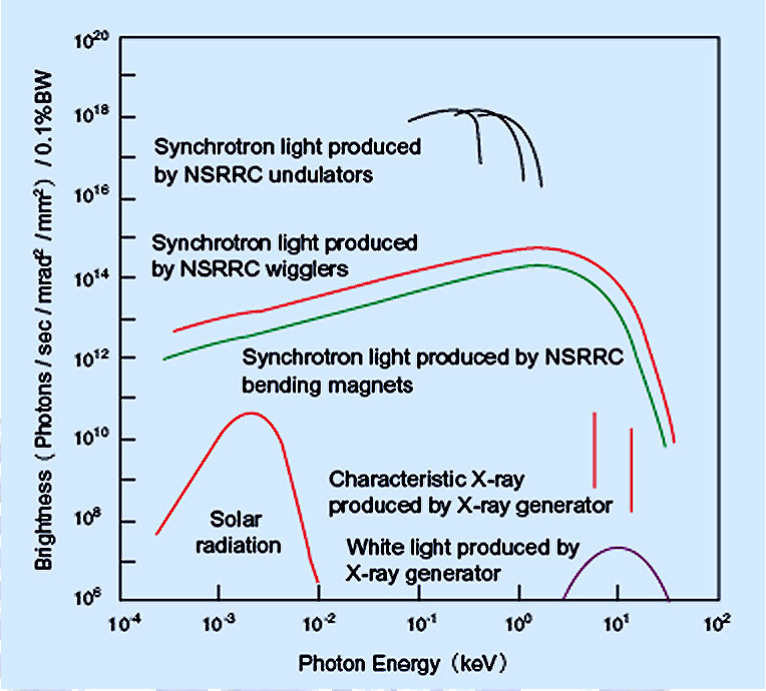

FIG 2.10: The bright spectra from NSRRC light sources, compared to traditional light sources.

2.4.2 *Extended X-ray absorption fine structure*

X-ray absorption fine structure refers to the details of how X-rays are absorbed by an atom at energies near and above the core-level binding energies of that atom, which provides structural information about a sample by way of the analysis of its X-ray absorption spectrum. The X-ray absorption spectrum is typically divided into two regimes: X-ray absorption near-edge spectroscopy (XANES) and extended X-ray absorption fine structure spectroscopy (EXAFS).

XANES is strongly sensitive to formal oxidation state and coordination chemistry (e.g., octahedral, tetrahedral coordination) of the absorbing atom, while the EXAFS is used to determine the distances, coordination number, and species of the neighbors of the absorbing atom.

Because of this dependence, EXAFS provides a practical, and relatively simple, way to determine the chemical state and local atomic structure for a selected atomic species. EXAFS can be used in a variety of systems and bulk physical environment and is routinely used in a wide range of scientific fields, including material science, biology, environmental science, and catalysts research.

Since EXAFS is an atomic probe, it places few constraints on the samples that can be studied. All atoms have core level electrons, EXAFS spectra can therefore be measured for essentially every element on the periodic table. Importantly, long-range ordered crystallinity is not absolutely necessary for EXAFS measurements, making it one of the few structural probes available for nanocrystalline and highly disordered materials [9], including solutions. Furthermore, EXAFS does not require any particular experimental conditions, such as vacuum (at least in principle). Because X-rays are fairly penetrating in matter, EXAFS is not inherently surface-sensitive, though special measurement techniques can be applied to enhance its surface sensitivity.

2.4.3 *X-Ray absorption and fluorescence measurements*

At the energy regime of X-rays, light is absorbed by all matter through the photoelectron effect. In this process, an x-ray photon is absorbed by a tightly bound electron in the core level (such as the 1*s* or 2*p* level) of an atom. If the

energy of X-rays is larger than the binding energy of the electron, the electron may be removed from its quantum level. In this case, the X-ray is absorbed and any energy in excess of the electronic binding energy is given to the kinetic energy of a photoelectron ejected from the atom.

The absorption coefficient, μ, for an atom is directly proportional to the probability of absorption of one photon and is a monotone decreasing function of energy. The Lambert-Beer law relates intensities I_0 and I to the absorption coefficient:

$$I = I_0 e^{-\mu t}, \tag{2.6}$$

where I is the intensity transmitted through the sample, I_0 is the X-ray intensity incident on a sample, and t is the sample thickness, as shown in Fig 2.11. For X-rays, the intensity is proportional to the number of X-ray photons. At most X-ray energies, the absorption coefficient μ is a smooth function of energy, with a value that depends on the sample density ρ, the atomic number Z, atomic mass A, and the X-ray energy E roughly as $\mu \approx \frac{\rho Z^4}{AE^3}$.

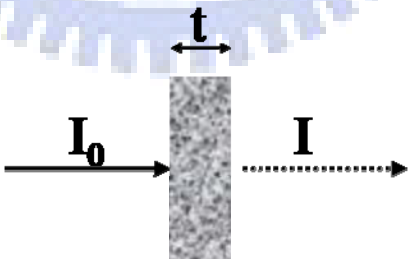

FIG. 2.11: X-ray absorption measurements: An incident beam of monochromatic X-rays of intensity I_0 passes through a sample of thickness t, and the transmitted beam has intensity I.

The absorption coefficient μ is strongly dependent on both Z and E, which is a fundamental property of X-rays. Due to the Z^4 dependence, the absorption

coefficients for distinct elements are quite different (spanning several orders of magnitude), so that good contrast between different materials can be achieved for nearly any sample thickness and concentrations by adjusting the X-ray energy. Figure 2.12 shows μ/ρ as a function of X-ray energy for Cd and Se. They have several discontinuities known as absorption edges, which occur when the energy of the incident photons equals the binding energy of one electron of the atom and are classified with capital letters (K, L, M…) according to the principal quantum number of the electron in the ground state (n=1, 2, 3…).

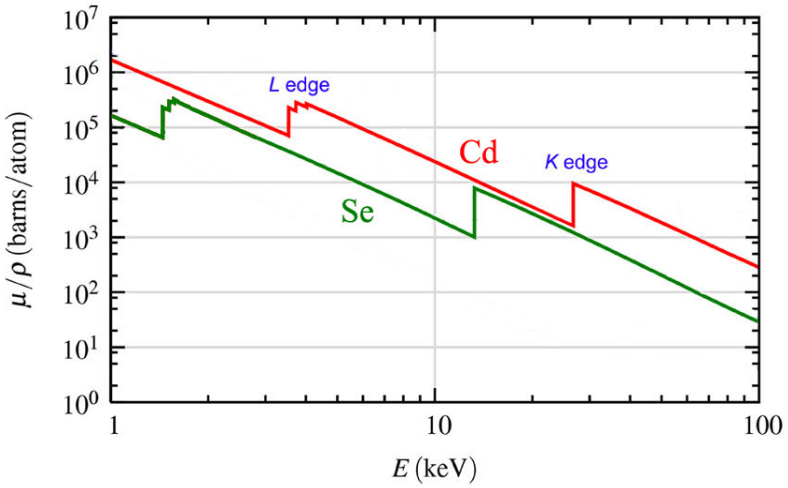

FIG. 2.12: The absorption cross-section μ/ρ for Cd and Se over the x-ray energy range of 1 to 100 keV [10]. Notice that there are at least 5 orders of magnitude in variation in μ/ρ, and that in addition to the strong energy dependence, there are also sharp rises corresponding to the core-level binding energies of the atoms.

For EXAFS, we are concerned with the intensity of μ as a function of energy, near and at energies just above these absorption edges. An EXAFS measurement is simply a measure of the energy dependence of μ at and above the binding energy of a known core level of a known atomic species. Every atom has core-level electrons with well-defined binding energies, we can thus select the

element to probe by tuning the X-ray energy to an appropriate absorption edge. These absorption edge energies are well-known and tabulated. The edge energies vary with atomic number approximately as Z^2, but both *K* and *L* levels can be used in the hard x-ray regime (in addition, *M* edges can be for heavy elements in the soft x-ray regime), which allows most elements to be probed by XAFS with x-ray energies between 5 and 35 keV. Because the element of interest is chosen in the experiment, EXAFS is *element-specific*.

EXAFS can be measured either in transmission or fluorescence geometries (The geometry for Auger measurements is typically the same as for fluorescence). One can measure the energy dependence of the absorption coefficient μ(E) either in transmission as

$$\mu(E) = \ln(I_0 / I) \tag{2.7}$$

or in X-ray fluorescence (or Auger emission) as

$$\mu(E) \propto I_f / I_0, \tag{2.8}$$

where I_f is the monitored intensity of a fluorescence line (or, again, electron emission) associated with the absorption process.

2.4.4 *EXAFS experiments*

Cd and Se *K*-edge EXAFS measurements were carried out at BL01C1 and BL17C1 at National Synchrotron Radiation Research Center (NSRRC) in Taiwan, respectively. NC samples were coated onto the scotch tape with the solvent being evaporated, and the tape was then folded several times to reach an appropriate thickness. The EXAFS spectra were collected in fluorescence mode (Fig. 2.13). The system was incorporated a closed-cycle liquid helium cryostat

to measure the low-temperature EXAFS data (~10 K). All reference materials such as bulk CdSe and CdO were prepared using the same process and measured under the similar conditions. The reference compounds served to determine the reduction factor S_0^2 of the EXAFS amplitude for Cd−Se and Cd−O pairs. The photon energies were calibrated with Cd foil or Se powder, which was placed downstream the sample and measured simultaneously. Standard procedures were followed to analyze the EXAFS data, including pre-edge and post-edge background subtraction, normalization with respect to the edge jump, Fourier transformation, and curve fitting. All computer programs are implemented in the UWXAFS 3.0 package. The phase shift and backscattering amplitude functions for specific atom pairs were *ab-intio* calculated by using the FEFF6 code.

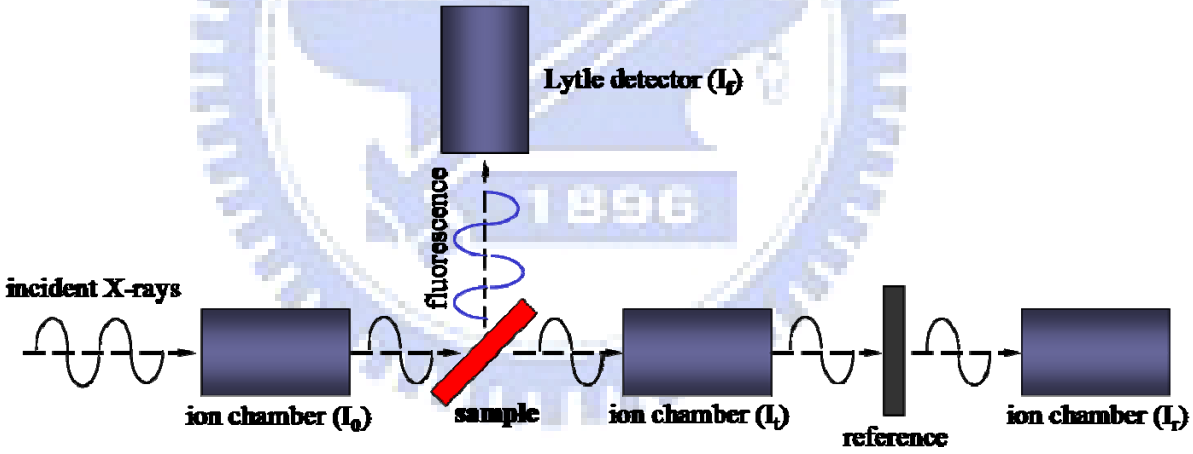

FIG. 2.13: Schematic representation of the set-up for EXAFS measurements using synchrotron radiation.

2.4.5 *EXAFS data treatment*

A typical EXAFS spectrum of CdSe powder sample (transmission geometry) is shown in Fig 2.14. The sharp rise in $\mu(E)$ due to the Se 1*s* electron level (at

12658 eV) is clearly visible in the spectra, as are the oscillations in $\mu(E)$ that are the EXAFS. As mentioned above, the EXAFS is generally thought of in two distinct portions: the near-edge spectra (typically within 30eV of the main absorption edge) and the extended fine-structure. The basic physical description of these two regimes is the same, but some important approximations and limits allow us to interpret the extended spectra in a more quantitative way than is currently possible for the near-edge spectra.

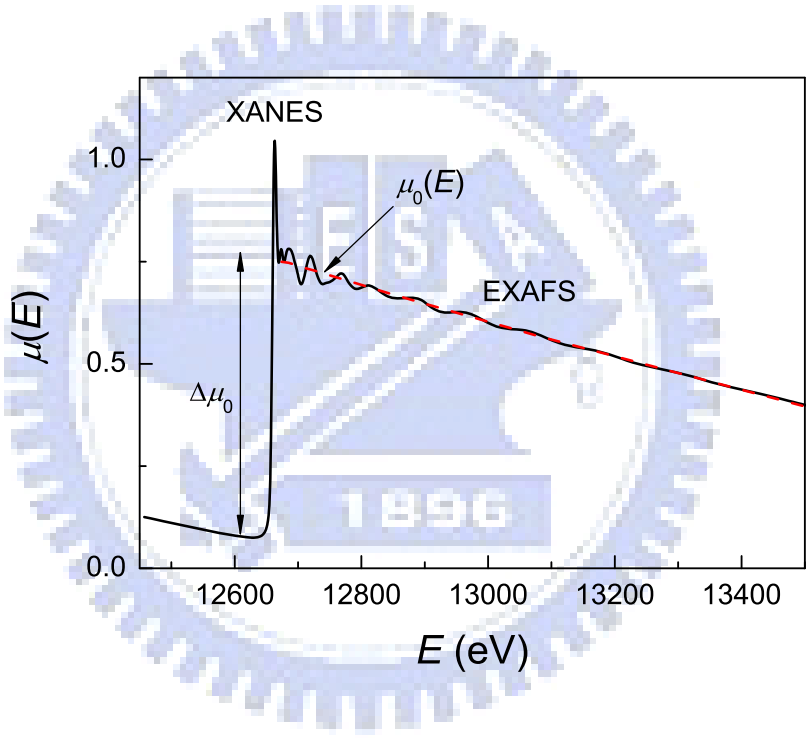

FIG. 2.14: Se *K*-edge EXAFS spectrum of bulk CdSe. The measured X-ray absorption spectrum is shown with the XANES and EXAFS regions identified. $\mu(E)$ is shown with smooth background function $\mu_0(E)$ and the edge-step $\mu_0(E_0)$.

The EXAFS fine-structure function $\chi(E)$ [8,10] is define as

$$\chi(E) = \frac{\mu(E) - \mu_0(E)}{\Delta\mu_0(E)}, \tag{2.9}$$

where $\mu(E)$ is the measured absorption coefficient, $\mu_0(E)$ is a smooth background function representing the absorption of an isolated atom, and $\Delta\mu_0$ is the

measured jump in the absorption $\mu(E)$ at the threshold energy E_0 (see Fig 2.14).

EXAFS is best understood in terms of the wave behavior of the photo-electron created in the absorption process. Because of this, it is common to convert the x-ray energy to k, the wave number of the photoelectron, which has dimensions of 1/distance and is defined as $k = \sqrt{2m(E - E_0)/\hbar^2}$, where E_0 is the absorption edge energy and m is the electron mass. If the absorbing is isolated in space, the photoelectron propagates as an unperturbed isotropic wave (Fig. 2.15 left), but in most cases there are many other atoms around the absorber. These become scattering centers of the photoelectron wave (Fig. 2.15 right). The final state of the photoelectron can be described by the sum of the original and scattered waves [11]. This leads to an interference phenomenon that modifies the interaction probability between core electrons and incident photons.

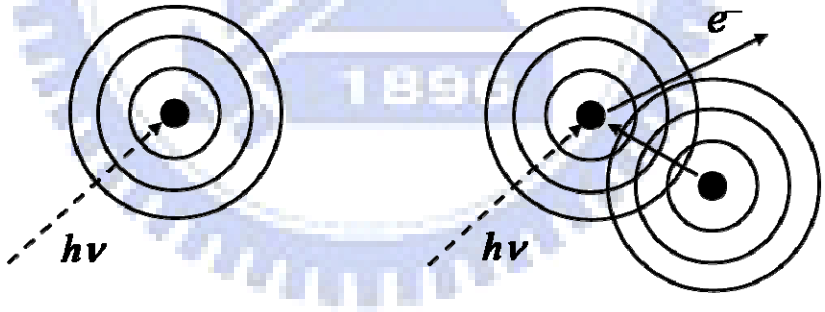

FIG. 2.15: Schemes of scattering processes.

The primary quantity for EXAFS is $\chi(k)$, the oscillations as a function of photoelectron wave number, and $\chi(k)$ is often referred to simply as "the EXAFS". In this way, the EXAFS extracted from the Se K-edge for CdSe is shown in Fig 2.16 (top); the EXAFS is oscillatory and decays quickly with k. To order to emphasize the oscillations, $\chi(k)$ is often multiplied by a power of k

typically k^2 or k^3, as shown in Fig 2.16 (bottom).

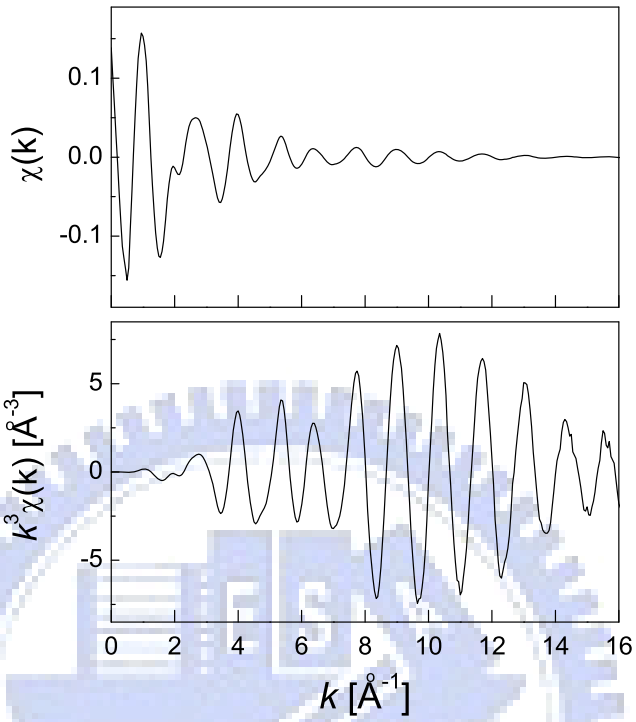

FIG. 2.16: Se *K*-edge EXAFS *k*- and k^3-weighted spectra of bulk CdSe.

The different frequencies apparent in the oscillations in $\chi(k)$ correspond to different near-neighbor coordination shells which can be described and modeled according to the EXAFS Equation [11],

$$\chi(k) = S_0^2 \sum_i \frac{N_i |f_i(k)|}{kR_i^2} \exp\left(-2\sigma^2 k^2\right) \exp\left(\frac{-2R_i}{\lambda(k)}\right) \sin[2kR + \Phi_i(k)], \qquad (2.10)$$

where S_0^2 is an average amplitude reduction factor, N_i is the number of atoms of type i at distance R_i from the absorber, $f_i(k)$ is a scattering amplitude function characteristic of the i-th atom, k is the wave vector modulus for the photoelectron, $\exp(-2\sigma^2k^2)$ considers the fluctuations of distances due to a structural and/or thermal disorder, $\exp[-2R_i/\lambda(k)]$ takes account of the finite elastic mean free paths of photoelectrons $\lambda(k)$, and $\Phi_i(k)$ is a phase function that

takes account of the varying potential field along which the photoelectron moves. The EXAFS equation allows us to determine N, R, and σ^2 knowing the scattering amplitude $f_i(k)$ and phase shift $\Phi_i(k)$. Furthermore, since these scattering factors depend on the Z of the neighboring atom, EXAFS is also sensitive to the atomic species of the neighboring atom.

2.5 Photoemission spectroscopy

Photoemission spectroscopy is an analytical technique based on the photoelectric effect, in which a sample is irradiated with photons and the emitted photoelectrons are studied. This technique has been established as one of the most important methods to study the electronic structure of molecules, solids and surfaces.

The photoelectric effect was discovered by Hertz in 1887 and theoretically described by Einstein in 1905. The first X-ray induced PES was developed by Robinson in 1913. The work was continued to the 1930's but low-energy resolution of electron spectrometers gave scientists difficulties to analyze results during that time. Thus, the method was not useful until high-resolution electron spectrometers became available so as to give unique information of the energy distribution of the emitted photoelectrons. High-resolution spectrometers were then developed in the mid-1950's by Kai Siegbahn and his research group. The method is since then called Electron Spectroscopy for Chemical Analysis (ESCA); the term ESCA was used because it was associated with the chemical state. The technique uses X-rays for irradiation is also known as X-ray photoelectron spectroscopy (XPS) and the name is now favored due to the

development of many electron spectroscopies. A related method called Ultraviolet photoelectron spectroscopy (UPS) uses ultraviolet radiation. The use of X-rays for excitation permits both core and valence electrons to be probed while ultraviolet radiation probes the outer valence electrons.

Today, the use of synchrotron radiation for the excitation of photoelectrons has become increasingly important because it allows measurements that cannot be performed with usual vacuum ultraviolet or X-ray sources in the laboratory. Many dedicated synchrotron facilities have been installed worldwide appropriate for PES experiments. The main difference compared to laboratory sources is that the photon energy can be selected by use of a monochromator from a continuous spectrum over a wide energy range. Other important advantages of the synchrotron light are, e.g., high intensity and brightness, variable polarization, small photon spots, or the possibility of time-resolved measurements on a very short timescale in the nanosecond range or even below.

2.5.1 *Principle*

Photoelectric effect can in principle be described by a simple process: electrons are excited and can leave the matter after the absorption of energy from electromagnetic radiation. Applying the principle of energy conservation from the Einstein's photoelectric relation, the kinetic energy of the emitted photoelectrons can be estimated [12]:

$$h\nu = E^f - E^i + E_K , \tag{2.11}$$

where $h\nu$ is the incoming photon energy, E^f is the total energy of ion (final state), E^i is the total energy of electron (initial state), and E_K is the photoelectron's

kinetic energy. If the final state is an ion, the binding energy of the photoelectron can be defined as:

$$E_B^{vac} = E^f - E^i, \tag{2.12}$$

where E_B^{vac} is the binding energy of photoelectron with reference to the vacuum level of the sample. The binding energy of photoelectron is affected by the initial- and final-state configurations of element as previously shown in Eq. (2.12). Rewriting Eq. (2.11) for an *N*-electron system,

$$E^i(N) + h\nu = E^f(N-1,K) - E_K(1), \tag{2.13}$$

where *K* is one electron orbital *K* from which photoionization occurs. It is known that,

$$E_B^{vac}(K) = h\nu - E_K(1). \tag{2.14}$$

It follows that Eq. (2.12) can be rewritten as,

$$E_B^{vac}(K) = E^f(N-1,K) - E^i(N). \tag{2.15}$$

The binding energy is therefore not just the binding energy of the electrons in the ground state, but corresponds also to the final state.

The Koopman's theorem (KT) assumes that when an electron is removed from an *N*-electron system, the wave functions of all the other electrons are unchanged, that is, the remaining (*N*–1) electrons are frozen in their original distribution. However, in reality, the remaining electrons relax to a different energy state after photoemission and the core hole will influence the final state of the photoemitted electrons such that the KT seldom applies. Taking this relaxation energy (dE_{relax}) into account, the binding energies estimated with KT are thus greater than the value measured in PES [12]:

$$E_B^{vac}(K) = E_B^{vac}(K)^{KT} - dE_{relax}. \tag{2.16}$$

For solid samples, the Fermi level is usually used to be the reference energy level, which is considered as the highest occupied level in solid. A work function ϕ is defined as the energy needed to move the electron from the Fermi level to the vacuum level (see Fig. 2.17). Thus,

$$h\nu = E_B^F + \phi + E_K^i , \tag{2.17}$$

in which E_B^F is the binding energy of electron relative to the Fermi level.

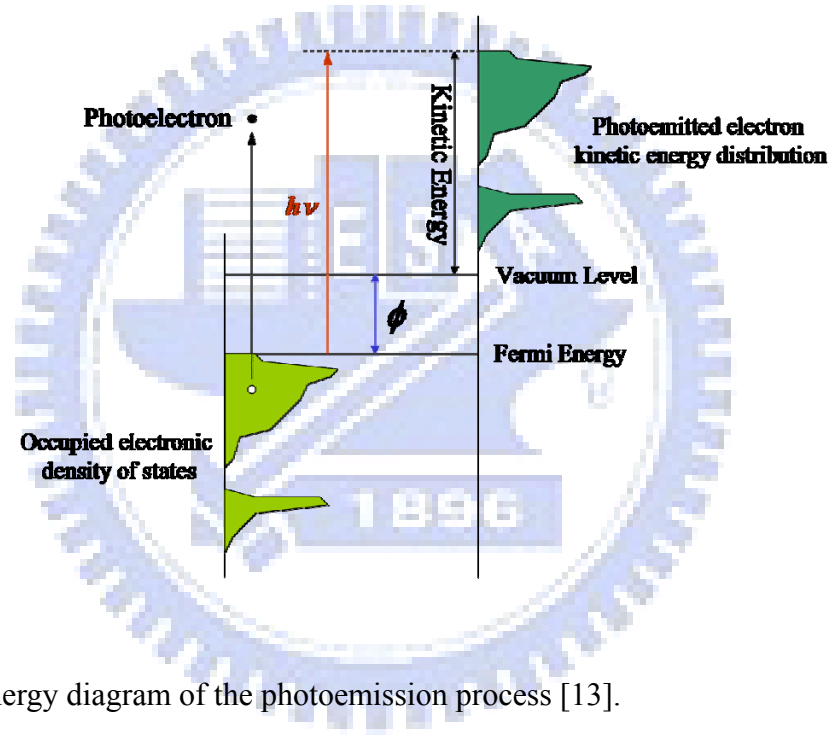

FIG. 2.17: Energy diagram of the photoemission process [13].

The kinetic energy measured by the spectrometer is related to the vacuum level of the spectrometer material. The work function for the spectrometer material must be introduced in the final equation:

$$h\nu = E_B^F + E_K + \phi_{sp} , \tag{2.18}$$

in which E_K is the measured kinetic energy and ϕ_{sp} is the work function for the spectrometer. During the measurement, if the photon energy and the

spectrometer work function are known, the binding energy of the photoelectrons can be derived from the kinetic energy of the emitted electrons relative to the Fermi level. The binding energy scale was derived to make uniform comparisons of the chemical states straightforward.

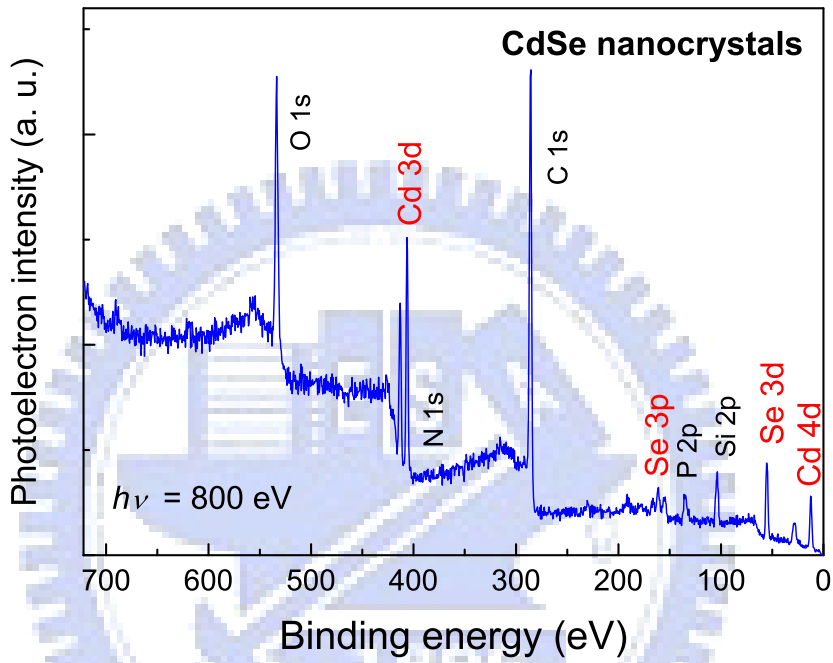

FIG. 2.18: Synchrotron photoemission spectrum of CdSe nanocrystals passivated with TOPO/HDA.

Both core- and valence-level electrons can be probed using X-rays as an excitation radiation. Core levels are defined as the inner quantum shells that do not participate in chemical bonding, while valence levels are electrons in the more weakly bound, partially filled outer quantum shells. The explanation to chemical identification is that core electrons are insensitive to their surroundings when condensed into a solid phase and retain the binding energies that are characteristics of the atom type. In Fig. 2.18, taking CdSe NCs as an example, the survey photoemission spectra by synchrotron radiation illustrate the electron

lines contributing from the Cd and Se signals at different levels and the presence of the carbon, oxygen, nitrogen, and phosphor signals from organic ligands (surfactants). The outermost electrons, which are directly involved in chemical bonding in a solid, are broadened in a 'valence band' and can effectively be probed using the UPS technique. Except for hydrogen, all elements can be detected and studied, because they have the characteristic core-level electrons even when combined with other elements to form a compound.

2.5.2 *Synchrotron photoemission experiments*

Photoemission experiments using synchrotron radiation were performed at beamlines BL-08A1 and BL-24A1 at NSRRC. BL-08A1 is a low-energy beamline with a spherical-grating monochromator (LSGM) that provides radiation with energy in a range 20−160 eV; we used it to measure valence-band and Se 3*d* core-level spectra. BL-24A1 is a wide-range beamline with a spherical-grating monochromator (WR-SGM) offering photons up to 1500 eV, which we used to measure Cd 3*d* core-level spectra.

All NC samples for the photoemission experiments were prepared on casting a dilute solution with dispersed NCs onto a tantalum foil; the solvent (toluene or pyridine) was allowed to evaporate under gaseous nitrogen. The samples were then transferred to the photoemission chamber within less than 10 min to minimize the possibility of oxidation. The photoemission spectra of samples thus prepared showed no oxidized components from contamination. Pure CdSe powder adhered to a Cu foil served as a bulk reference. All NC samples, a bulk sample and a gold foil were mounted on a grounded sample holder; to calibrate the binding energy, the Fermi level of gold served as a reference. A

hemispherical energy analyzer (Omicron EA-125) was used to collect photoelectrons at an overall resolution 0.05−0.1 eV. All photoemission spectra were collected in a normal emission geometry (Fig. 2.19); the base pressure in the chamber was maintained at 2×10^{-9} Torr during the measurements.

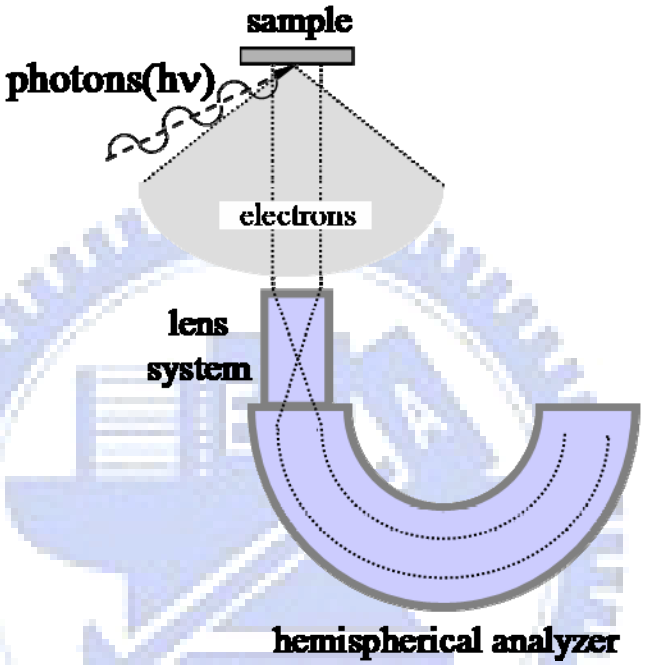

FIG. 2.19: Schematic diagram of photoemission experiment.

2.6 References

[1] Meng-Ting Hsieh, *Synthesis and characterization of CdSe, CdSe/ZnS, and CdSe/ZnSe quantum dots*, MD thesis, Department of Material Science and Engineering, National Chiao Tung University (2004).

[2] C. B. Murray, D. J. Norris, and M. G. Bawendi, J. Am. Chem. Soc. **115**, 8706 (1993).

[3] P. Reiss, J. Bleuse, and A. Pron, Nano Lett. **2**, 781 (2002).

[4] W. W. Yu, L. Qu, W. Guo, and X. Peng, Chem. Mater. **15**, 2854 (2003).

[5] A. Guinier, *X-Ray Diffraction*: *In Crystals, Imperfect Crystals, and Amorphous Bodies* (Dover Publications, New York, 1994).

[6] R. L. Snyder, J. Fiala, and H. J. Bunge, *Defect and Microstructure Analysis by Diffraction* (Oxford University Press Inc., New York, 1999).

[7] B. E. Warren, *X-ray Diffraction* (Addison-Wesley, 1969).

[8] J. Als-Nielsen and D. McMorrow, *Elements of Modern X-ray Physics* (John Wiley & Sons Ltd, England, 2001).

[9] F. Z. Chien, S. C. Moss, K. S. Liang, and R. R. Chianelli, Phys. Rev. B **29**, 4606 (1984).

[10] M. Newville, *Fundamentals of XAFS* (Chicago, 2004).

[11] G. Vlaic and L. Olivi, Croat. Chem. Acta **77**, 427 (2004).

[12] R. M. Petoral, *Photoelectron spectroscopy applied to molecular surface science* (2005).

[13] A. Zangwill, *Physics at Surfaces* (Cambridge, 1988).